

Emergent gauge flux and spin ordering in magnetized triangular spin liquids: applications to Hofstadter-Hubbard model

Jiahao Yang (杨家豪)¹ Hao Tian ¹ Si-Yu Pan ¹ and Gang v. Chen ^{1, 2, *}

¹International Center for Quantum Materials, School of Physics, Peking University, Beijing 100871, China

²Collaborative Innovation Center of Quantum Matter, 100871, Beijing, China

(Dated: January 21, 2026)

Motivated by the recent progress in the moiré superlattice systems and spin-1/2 triangular lattice antiferromagnets, we revisit the triangular-lattice spin liquids and study their magnetic responses. While the magnetic responses on the ordered phases can be mundane, the orbital magnetic flux and the Zeeman coupling have synergetic effects on the internal gauge flux generations in the relevant spin liquid phases. The former was known to induce an internal U(1) gauge flux indirectly through the charge fluctuations and ring exchange, and thus could lead to the formation of a chiral spin liquid. The latter could spontaneously generate a uniform field-dependent internal gauge flux, driving a conically-ordered state. The competition and interplay between these two field effects are discussed through a generic spin-1/2 J_1 - J_2 - J_χ model and with the experimental consequences. Our results could find applications in the moiré superlattice systems with the Hofstadter-Hubbard model as well as the triangular lattice antiferromagnets.

Introduction.—Historically, the induction of the internal gauge flux by the orbital magnetic field has been proposed to predict the quantum oscillation behaviours in the weak Mott insulating triangular lattice spin liquids [1, 2]. It is understood that, the variation of the external orbital magnetic flux leads to the variation of the internal gauge flux for the fermionic spinons and then the successive occupation of the spinon Landau levels. The integer-filled spinon Landau level states are in fact chiral spin liquids (CSLs), and the quantum oscillation is the successive appearance of CSLs that are tuned by the orbital magnetic field. Due to various constraints such as small lattice constants, the generation of CSLs in the triangular lattice Mott insulating systems have not yet been achieved. In the era of moiré physics, the triangular lattice Hubbard model has been proposed to realize in transition metal dichalcogenide moiré systems [3, 4], and the large moiré lattice constants allow a large orbital magnetic flux through the moiré unit cell. The resulting model is referred as the triangular lattice Hofstadter-Hubbard (HH) model, and the orbital field-induced CSL in the weak Mott regime becomes experimentally feasible [5–7].

In the existing study of the triangular lattice HH model, the Zeeman coupling of the magnetic field is often ignored. This is because the strong field polarizes the spin completely and the layer index is used as an effective spin. In this Letter, however, we include the Zeeman coupling in the modelling, and consider the interplay and competition between the orbital magnetic flux and Zeeman coupling in the relevant spin liquids. In addition to the moiré systems, the triangular lattice antiferromagnets have experienced a great development in recent years, ranging from the rare-earth magnets [8–11] to the Cobalt-based magnets [12–15], where many interesting and exotic physics have been proposed. These materials are in the strong Mott regime, and the underlying

models are simply pairwise spin interactions. To incorporate both the moiré systems and the emerging strong Mott-insulating triangular lattice antiferromagnets, we consider a spin- $\frac{1}{2}$ J_1 - J_2 - J_χ model in a Zeeman magnetic field, where the effect of the orbital magnetic flux is encoded in the scalar spin-chirality term J_χ [16].

Model.—The J_1 - J_2 - J_χ spin model is given as

$$\mathcal{H} = J_1 \sum_{\langle ij \rangle} \mathbf{S}_i \cdot \mathbf{S}_j + J_2 \sum_{\langle\langle ij \rangle\rangle} \mathbf{S}_i \cdot \mathbf{S}_j + J_\chi \sum_{\Delta} \mathbf{S}_i \cdot (\mathbf{S}_j \times \mathbf{S}_k), \quad (1)$$

where J_1 (J_2) is the first (second) neighbor spin interaction and is set to be antiferromagnetic, and J_χ is a scalar spin chirality term in Fig. 1(a). The spin chirality term can be obtained from the third-order perturbation of the HH model in the Mott regime and thus experiences the orbital magnetic flux ϕ_Δ through the triangular plaquette with $J_\chi \propto \sin \phi_\Delta$ [1, 16–18]. This chirality term can be neglected for the strong Mott insulators. Because this model preserves the spin rotational symmetry, the remaining Zeeman coupling can be applied in any direc-

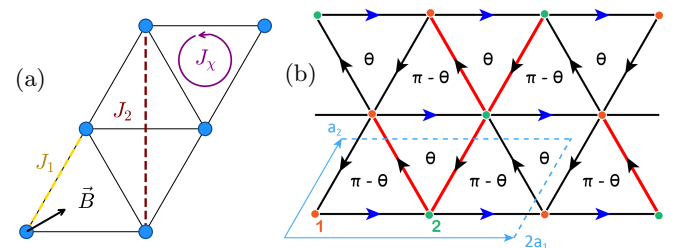


FIG. 1. (a) Schematic illustration of the triangular lattice J_1 - J_2 - J_χ model under a magnetic field \vec{B} . (b) The $[\theta, \pi - \theta]$ state with staggered θ flux. The phase $e^{i\phi_{ij}}$ takes $\phi_{ij} = \mp\theta$ when the spinon hops parallel (antiparallel) to the blue arrows, and $\phi_{ij} = 0$ when the spinon hops along black arrows. For the red lines, ϕ_{ij} further acquires a phase of π .

tion, and we set it to the z direction with $-B \sum_i S_i^z$.

The phase diagram of this model has been known from early studies [19, 20]. With $J_\chi = 0$, the system realizes the $\sqrt{3} \times \sqrt{3}$ (the stripe) ordered state for $J_2/J_1 \lesssim 0.08$ ($J_2/J_1 \gtrsim 0.15$), and a U(1) Dirac spin liquid (DSL) in the intermediate parameter regime ($0.08 \lesssim J_2/J_1 \lesssim 0.15$). With a non-zero J_χ , a large parameter region turns into the CSL. The orbital flux is responsible for the formation of the CSL in this model. The physics about the ordered states are somewhat well-understood. We here focus on the magnetic responses of the two spin liquid states and provide feedback to their experimental detection.

Triangular Spin liquids.—To capture the dominant physics of spin liquids of Eq. (1), we introduce Abrikosov fermionic operators $f_{i\alpha}$, with $\alpha = \uparrow, \downarrow$ being the spin up and down index. The spin-1/2 operators can be expressed as the fermion bilinears $S_i^a = \frac{1}{2} \sum_{\alpha\beta} f_{i\alpha}^\dagger \sigma_{\alpha\beta}^a f_{i\beta}$, where $\sigma^a (a = x, y, z)$ are three Pauli matrices. The physical Hilbert space is restored by imposing a local single-occupancy constraint, $\sum_\alpha f_{i\alpha}^\dagger f_{i\alpha} = 1$. Applying the parton mean-field decoupling, we obtain the spinon mean-field theory with [21],

$$H_{\text{MF}} = -t \sum_{\langle ij \rangle, \alpha} \left(e^{i\phi_{ij}} f_{i\alpha}^\dagger f_{j\alpha} + \text{h.c.} \right) - \mu \sum_{i\alpha} f_{i\alpha}^\dagger f_{i\alpha} - B \sum_{i\alpha\beta} \frac{1}{2} f_{i\alpha}^\dagger \sigma_{\alpha\beta}^z f_{i\beta}, \quad (2)$$

where hopping $t > 0$ and ϕ_{ij} is bond-dependent phase factor (see Fig. 1(b)).

The total flux enclosed within a single triangular plaquette is obtained by moving the spinon anticlockwise along three edges of the triangle. In Fig. 1(b), we choose the flux configuration $[\theta, \pi - \theta]$ with the down-triangle flux $\phi_\nabla = \theta$, and the up-triangle flux $\phi_\Delta = \pi - \theta$. The total number of spinons and the magnetization are controlled by the chemical potential μ and the Zeeman field B , respectively. When $\theta = 0$, the system is described by the U(1) DSL state with the $[0, \pi]$ flux configuration. The scalar spin-chirality term J_χ in Eq. (1) induces a staggered gauge flux distribution with $\theta \neq 0$ on top of the $[0, \pi]$ flux configuration, thereby driving the emergence of a CSL state with the $[\theta, \pi - \theta]$ flux configuration [22].

We analyze the spinon band evolution of Eq. (2) for the flux configuration $[\theta, \pi - \theta]$. With $\theta = 0$, the ground state exhibits the well-known U(1) DSL state with a spectrum featuring a pair of Dirac cones for each spinon species in Fig. 2(a). Upon introducing a non-zero staggered flux θ , the system transitions into a CSL phase breaking both time-reversal and parity, while maintaining the combined symmetry of the two. The introduction of non-zero θ leads to the emergence of a direct gap at each Dirac cone [see Fig. 2(b)]. The lower band is fully occupied, while the upper band remains empty, maintaining the half-filling condition. We find that the filled (empty) band has non-zero Chern numbers with values

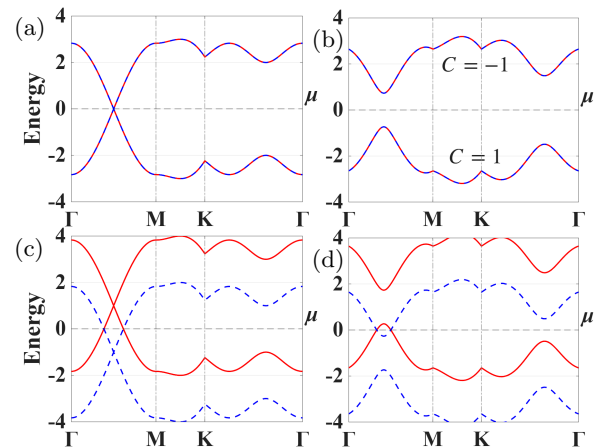


FIG. 2. Spinon dispersions of the $[\theta, \pi - \theta]$ state along high-symmetry lines in the Brillouin zone. (a) DSL with $\theta = 0$ and (b) CSL with $\theta = \pi/6$ at zero field. The dispersions for DSL (c) and CSL (d) with $B = 2$. A finite staggered flux θ gaps out the Dirac cone in (a), and the resulting bands acquire non-zero Chern numbers. The finite B splits the spin- \uparrow (blue dashed line) and spin- \downarrow (red solid line) bands, leading to Fermi-pocket states with finite magnetizations in (c) and (d).

of $C = 1(-1)$. Taking into account the spin degeneracy, the net Chern number of the occupied bands amounts to $+2$, corresponding to a CSL phase. Consequently, the resulting fully gapped bands exhibit topologically non-trivial characteristics such as the thermal Hall response as we will discuss in the following.

A finite Zeeman field B lifts the spin degeneracy of the spinon bands and generates Fermi-pocket (FP) states in both the DSL and CSL phases in order to maintain half-filling, thereby inducing a finite magnetization, as shown in Fig. 2(c) and (d), respectively. For the CSL, the field-induced spin splitting needs to overcome the spinon gap to generate the spinon Fermi pockets. Otherwise, the CSL is robust. At this stage, the scalar spin chirality, that is generated by the orbital magnetic flux, converts the DSL into the CSL, and the Zeeman field converts the DSL into the FP state. They have different effects even from this simple treatment.

Spinon Landau level and spin ordering.—Under the Zeeman coupling, the system first develops a FP state with spin-split spinon Fermi surfaces and a finite magnetization. This state hosts gapless spinon excitations and is, in general, energetically unstable. It has been argued that the Zeeman-induced spin imbalance renders the FP state unstable toward a state with spontaneously generated internal U(1) gauge flux, which reorganizes the Dirac spinons into Landau levels and gaps them in the kagomé lattice antiferromagnets [see Fig. 3(a)] [23, 24]. Extending this understanding to the triangular lattice, a low-energy continuum theory shows that the LL state is energetically favorable compared to the FP state in the presence of a finite uniform internal gauge flux and mag-

netization [16]. In this picture, the spontaneously generated internal U(1) gauge flux is superimposed on the background flux of the DSL or CSL state, yielding the LL state with a mean-field phase diagram shown in Fig. 3(b) [16]. In the resulting magnetized spinon LL state, the occupied spin- \uparrow Landau levels carry a total Chern number $C_\uparrow = +1$, while the occupied spin- \downarrow Landau levels carry $C_\downarrow = -1$, yielding a vanishing net Chern number. Thus, the remaining low-energy dynamics is governed by the Maxwell gauge field since the Chern-Simons term is absent. A 2π gauge-flux insertion carries $\Delta S^z = 1$, identifying the monopole operator with a lattice S^+ operator. By the U(1) gauge-XY duality, long-range order of monopole operators corresponds to spontaneous breaking of the residual S^z -U(1) symmetry, resulting in coplanar XY spin ordering [21, 25].

To demonstrate this LL instability and the resulting spin ordering in our triangular lattice system, we perform the Gutzwiller-projected Monte Carlo calculations with gauge fluctuations included [16, 26, 27]. We construct the projected wave function $|\Psi_{\text{prj}}(\{\chi_{ij}\})\rangle = P|\Psi_{\text{MF}}(\{\chi_{ij}\})\rangle$ where $P = \prod_i (1 - n_{i\uparrow}n_{i\downarrow})$ being the Gutzwiller projector and $|\Psi_{\text{MF}}(\{\chi_{ij}\})\rangle$ is the mean-field wavefunction of the Hamiltonian Eq. (2). We then consider different gauge flux configurations $\{\chi_{ij}\}$ to calculate the energy of Eq. (1) under different magnetization. On a 18×18 lattice, the energetics of the FP and LL states are shown in Fig. 4(a), where the LL state exhibits lower energy than the FP state across a range of magnetization densities m_z as expected from the continuum theory. Furthermore, we compute the transverse spin structure factor ,

$$S^{XY}(\mathbf{q}) = \frac{1}{N} \sum_{i,j} e^{i\mathbf{q} \cdot (\mathbf{r}_i - \mathbf{r}_j)} \langle S_i^x S_j^x + S_i^y S_j^y \rangle, \quad (3)$$

for the projected LL state at $m_z \approx 0.05$ in Fig. 4(b). The

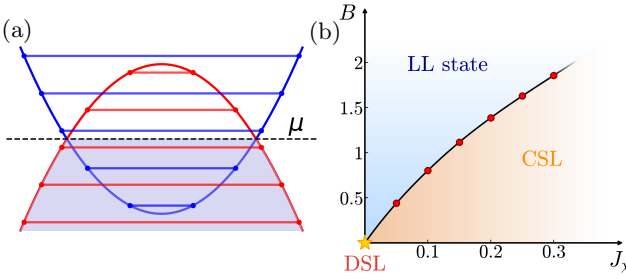


FIG. 3. (a) Schematic evolution from a Zeeman-split Fermi pocket (FP) state to a Landau-level (LL) state at finite magnetization. Blue and red parabolic bands (discrete levels) represent spin- \uparrow and spin- \downarrow spinons, respectively. The dashed horizontal line refers to the chemical potential. (b) Mean-field J_x - B phase diagram with fixed $J_1 = 1$, $J_2 = 0.1$. At finite J_x , the DSL (yellow star) evolves into CSL at zero field, which remains stable up to a critical field B_c (red dots), beyond which it transitions into the LL state. The parameter θ for different J_x at the red dots are consistent with variational Monte Carlo results from Ref. [22].

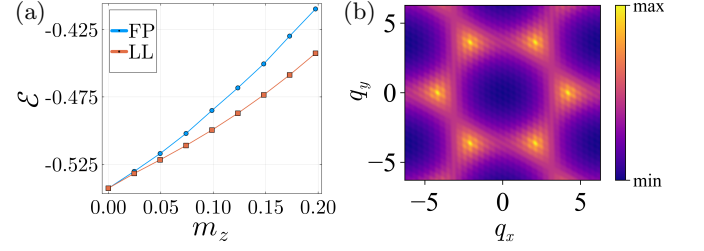


FIG. 4. Projected Monte Carlo results for the FP and LL states with $\theta = 0.1\pi$, $J_1 = 1$, $J_2 = 0.1$, and $J_x = 0.3$ on a 18×18 lattice. (a) Energy density \mathcal{E} as a function of magnetization density m_z . (b) Spin structure factor $S^{XY}(\mathbf{q})$ for projected LL state at $m_z \approx 0.05$, where prominent peaks appear at the K points of the Brillouin zone.

$S^{XY}(\mathbf{q})$ has prominent peaks at the K points, suggesting the 120° spin order and thus a conically-ordered state. The spin rotation symmetry breaking with the ordering vector at the K point also marks the emergence of the gapless Goldstone modes of the U(1) spin rotation symmetry.

Thermal Hall effect.—The thermal Hall effect, capable of probing the topology of the spinon bands, has proven valuable for investigating the topological characteristics of the fractionalized spinons in both experiment and theory. The thermal Hall conductivity for a fermionic system at finite chemical potential μ is given by [28],

$$\kappa_{xy} = -\frac{k_B^2}{\hbar T} \int d\epsilon (\epsilon - \mu)^2 \sigma_{xy}(\epsilon) \frac{\partial f(\epsilon, \mu, T)}{\partial \epsilon} \quad (4)$$

where $f(\epsilon, \mu, T) = [e^{(\epsilon - \mu)/k_B T} + 1]^{-1}$ is the Fermi function, and $\sigma_{xy}(\epsilon) = -\sum_{n, \epsilon_{nk} < \epsilon} \Omega_{nk}(\epsilon_{nk})$ denotes (\hbar/e^2) times the zero-temperature anomalous Hall coefficient evaluated at chemical potential ϵ . The Berry curvature Ω_{nk} is defined as Kubo-like formula. By enforcing the single-site spinon occupancy constraint, the chemical potential μ is fixed such that the system remains at half-filling. The Chern number of the n -th band is defined as $C_n = \frac{1}{2\pi} \int d^2k \Omega_{nk}$. For an isolated band, separated from all others by an energy gap, the Chern number is well defined and necessarily an integer. In the zero-temperature limit, Eq. (4) reduces to the Wiedemann-Franz form,

$$\left. \frac{\kappa_{xy}}{T} \right|_{T \rightarrow 0} = -2 \times \frac{\pi k_B^2}{6\hbar} \sum_{n \in \text{filled bands}} C_n, \quad (5)$$

where the prefactor of 2 accounts for spin degeneracy. This result implies that, at $T = 0$, κ_{xy}/T is quantized in integer multiples of $\pi k_B^2/6\hbar$. Moreover, Eq. (4) directly relates the thermal Hall conductivity κ_{xy} to the momentum-space distribution of Berry curvature.

In the DSL with gapless Dirac cones, the Brillouin-zone-integrated Berry curvature weighted by occupation vanishes identically due to the presence of both time-reversal and inversion symmetries, resulting in a zero

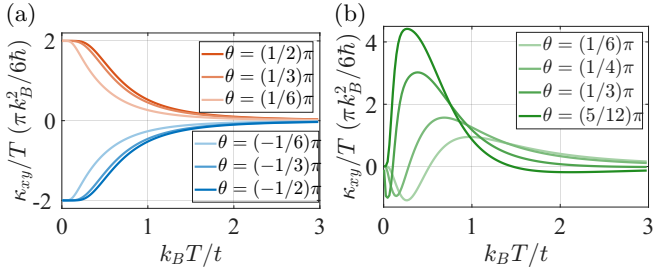


FIG. 5. Temperature dependence of the spinon thermal Hall conductivity κ_{xy}/T in units of $\pi k_B^2/6\hbar$. (a) Results for the CSL at $B = 0$ and $\phi_u = 0$ for different staggered flux θ . As $T \rightarrow 0$, κ_{xy}/T approaches the quantized value ± 2 , and its magnitude decreases continuously toward zero with increasing temperature. (b) Results for the magnetized LL state at uniform flux $\phi_u = 2\pi/76$ and field $B = 1$. The κ_{xy}/T vanishes in the zero-temperature limit due to the cancellation of the Chern numbers from spin- \uparrow and spin- \downarrow sectors.

κ_{xy}/T . In the CSL with finite staggered flux θ , both symmetries are broken, leading to finite spin chirality and nonzero Berry curvature distribution in the momentum space. Therefore the CSL phase exhibits a non-trivial thermal Hall response, as shown in Fig. 5(a). In the CSL phase, the κ_{xy}/T is quantized to 2 in the zero-temperature limit, and the quantization persists upto a finite temperature due to the gauge-flux induced energy gap. It exhibits a monotonically rapid decrease due to thermal population of spinon bands with opposite Chern number as the temperature rises. At temperatures significantly surpassing the maximum energy of the spinon bands, all the bands are almost equally populated, and the summation of Berry curvatures of all bands vanishes, leading to the vanishing κ_{xy}/T . The sign effect of the phase θ is demonstrated. It is observed that the κ_{xy}/T acquires a minus sign correspondingly, which is related to the Chern number exchanges between the occupied and unoccupied bands.

We proceed to include the the spontaneously generated internal gauge flux from the finite Zeeman coupling B , and denote this uniform flux as ϕ_u . Consequently, the original spinon bands are split into a set of Hofstadter-like flat subbands, whose spin degeneracy is lifted by the Zeeman coupling [16]. Because of the finite magnetization, the resulting spin imbalance arranges the band fillings such that the occupied spin- \uparrow (spin- \downarrow) spinon bands carry a total Chern number of $+1$ (-1), yielding a vanishing net Chern number. In Fig. 5(b), we show that the thermal Hall conductivity κ_{xy}/T with $\phi_u = 2\pi/76$ and $B = 1$ indeed approaches zero in the zero-temperature limit, despite the CSL parent state with a finite θ before a finite field is applied. The temperature dependence of κ_{xy}/T , however, is non-monotonic. For small T , κ_{xy}/T first becomes negative and then rises sharply to positive values. This behaviour reflects the presence of Hofstadter subbands with negative Chern numbers lying

closest to the chemical potential, which becomes dominant at low temperatures. As the temperature is further increased, the subbands with larger positive Chern numbers enter and contribute to the response, producing a pronounced hump in κ_{xy}/T . At sufficiently high temperatures, all bands are thermally populated and their Berry-curvature contributions cancel, causing κ_{xy}/T to decay toward zero.

As θ approaches zero, the thermal Hall response diminishes gradually and vanishes entirely across all temperatures when $\theta = 0$. This occurs because contributions from spin- \uparrow and spin- \downarrow spinons can cancel each other at all temperatures in the LL state derived from the DSL at $\theta = 0$ [16]. Specifically, the total Hall coefficient σ_{xy}^{tot} is an odd function of energy due to the symmetric properties of the Berry curvatures. Upon integrating over energy with the remaining even-function factors in Eq. (4), the thermal Hall conductivity κ_{xy}/T vanishes identically at all temperatures. The distinct thermal Hall conductivity behaviors exhibited by the DSL, CSL, and LL states under combined effect of Zeeman field B and internal gauge flux ϕ_u thus provide useful experimental signatures to distinguish these exotic quantum states.

Discussion.—In moiré systems, Hofstadter physics with large and tunable orbital flux can emerge at experimentally accessible magnetic fields due to the large moiré lattice constants. These HH systems thus provide a promising platform to study the competition between orbital-field-induced Hofstadter bands and interaction-driven Mott physics, which can stabilize exotic phases such as CSLs [5, 6] and even superconductivity [29, 30]. Moreover, the role of Zeeman-field-induced magnetization in modifying spin-liquid states remains of great interest but is relatively less understood [18, 23]. For the rare-earth Yb-based and other Co-based triangular lattice antiferromagnets, the DSL physics has been proposed to be relevant [8–15, 31]. As these materials are in the strong Mott regime, the spin liquid physics arises from the pairwise competing interactions, and the flux term can be ignored.

The recent numerical works on similar triangular lattice reveal a field-induced transition from a U(1) DSL to a noncoplanar cone state with finite chirality [32] or possible monopole phase [33] with increasing magnetic field, which should be consistent with the LL-picture in present work. We further remark that the total thermal Hall conductance is zero at zero temperature for the LL state, and thus no Chern-Simons term is generated for the emergent gauge field. Consequently, the emergent gauge field remains gapless, leading to a gapless U(1) gauge photon mode in the low-energy spectrum. This gapless gauge photon can be interpreted as the Goldstone mode arising from the spontaneous breaking of the U(1) spin-rotation symmetry, and such photon mode is expected to be observed in the spin correlation functions at low energies, which can be probed in future neutron

scattering experiments.

Finally, the finite-temperature thermal disordered regime of the weakly ordered states, that is in proximity to the nearby spin liquid [31], is probably more appropriately described from the thermalized spin liquid. The magnetic field response and properties in this regime may then be understood from the thermalized LL states. It would be interesting to explore this direction numerically and experimentally.

To summarize, we investigate the triangular spin liquids using a parton mean-field approach that incorporates both the Zeeman effect and the internal U(1) gauge flux. We show that their combined effect drives an instability of the FP state and energetically stabilizes a LL state. This LL state endows a conical spin order from spontaneous symmetry breaking. This finding justifies a routine for finding the emergence of magnetic order in QSL systems under external Zeeman field. We present distinctive signatures of spinon thermal Hall effect in these spin states, which can serve as a useful probe for the future experiments.

Acknowledgments.—J.Y. thanks Xu-Ping Yao, Zheng-Xin Liu, Xuan-Zhe Xia for helpful discussions. This work is supported by NSFC with Grants No.92565110 and No.12574061, by the Ministry of Science and Technology of China with Grants No. 2021YFA1400300, and by the Fundamental Research Funds for the Central Universities, Peking University.

D. L. Quintero-Castro, L. W. Harriger, M. D. Frontzek, L. Hao, S. Meng, Q. Zhang, G. Chen, and J. Zhao, Evidence for a Spinon Fermi Surface in a Triangular-Lattice Quantum-Spin-Liquid Candidate, *Nature* **540**, 559 (2016).

- [9] Y. Shen, Y.-D. Li, H. C. Walker, P. Steffens, M. Boehm, X. Zhang, S. Shen, H. Wo, G. Chen, and J. Zhao, Fractionalized excitations in the partially magnetized spin liquid candidate YbMgGaO_4 , *Nat Commun* **9**, 4138 (2018).
- [10] R. Bag, S. Xu, N. E. Sherman, L. Yadav, A. I. Kolesnikov, A. A. Podlesnyak, E. S. Choi, I. da Silva, J. E. Moore, and S. Haravifard, Evidence of dirac quantum spin liquid in $\text{YbZn}_2\text{GaO}_5$, *Phys. Rev. Lett.* **133**, 266703 (2024).
- [11] H. C. H. Wu, F. L. Pratt, B. M. Huddart, D. Chatterjee, P. A. Goddard, J. Singleton, D. Prabhakaran, and S. J. Blundell, Spin Dynamics in the Dirac U(1) Spin Liquid $\text{YbZn}_2\text{GaO}_5$, *Phys. Rev. Lett.* **135**, 046704 (2025).
- [12] S. Lee, C. H. Lee, A. Berlie, A. D. Hillier, D. T. Adroja, R. Zhong, R. J. Cava, Z. H. Jang, and K.-Y. Choi, Temporal and field evolution of spin excitations in the disorder-free triangular antiferromagnet $\text{Na}_2\text{BaCo}(\text{PO}_4)_2$, *Phys. Rev. B* **103**, 024413 (2021).
- [13] R. Zhong, S. Guo, G. Xu, Z. Xu, and R. J. Cava, Strong quantum fluctuations in a quantum spin liquid candidate with a Co-based triangular lattice, *Proc. Natl. Acad. Sci. U.S.A.* **116**, 14505 (2019).
- [14] R. Zhong, S. Guo, and R. J. Cava, Frustrated magnetism in the layered triangular lattice materials $\text{K}_2\text{Co}(\text{SeO}_3)_2$ and $\text{Rb}_2\text{Co}(\text{SeO}_3)_2$, *Phys. Rev. Mater.* **4**, 084406 (2020).
- [15] M. Zhu, V. Romerio, N. Steiger, S. D. Nabi, N. Murai, S. Ohira-Kawamura, K. Yu. Povarov, Y. Skourski, R. Sibille, L. Keller, Z. Yan, S. Gvasaliya, and A. Zheludev, Continuum Excitations in a Spin Supersolid on a Triangular Lattice, *Phys. Rev. Lett.* **133**, 186704 (2024).
- [16] See Supplemental Material for more technical details and additional supporting results.
- [17] J.-Y. P. Delannoy, M. J. P. Gingras, P. C. W. Holdsworth, and A.-M. S. Tremblay, Néel Order, Ring Exchange, and Charge Fluctuations in the Half-Filled Hubbard Model, *Phys. Rev. B* **72**, 115114 (2005).
- [18] Y. Huang, D. N. Sheng, and J.-X. Zhu, Magnetic Field Induced Partially Polarized Chiral Spin Liquid in a Transition Metal Dichalcogenide Moiré System, *Phys. Rev. B* **109**, 165109 (2024).
- [19] S.-S. Gong, W. Zhu, J.-X. Zhu, D. N. Sheng, and K. Yang, Global phase diagram and quantum spin liquids in a spin- $\frac{1}{2}$ triangular antiferromagnet, *Phys. Rev. B* **96**, 075116 (2017).
- [20] A. Wietek and A. M. Läuchli, Chiral spin liquid and quantum criticality in extended $s = \frac{1}{2}$ heisenberg models on the triangular lattice, *Phys. Rev. B* **95**, 035141 (2017).
- [21] X.-G. Wen, *Quantum Field Theory of Many-Body Systems: From the Origin of Sound to an Origin of Light and Electrons* (Oxford University Press, USA, 2007).
- [22] W.-J. Hu, S.-S. Gong, and D. N. Sheng, Variational Monte Carlo study of chiral spin liquid in quantum antiferromagnet on the triangular lattice, *Phys. Rev. B* **94**, 075131 (2016).
- [23] Y. Ran, W.-H. Ko, P. A. Lee, and X.-G. Wen, Spontaneous Spin Ordering of a Dirac Spin Liquid in a Magnetic Field, *Phys. Rev. Lett.* **102**, 047205 (2009).
- [24] S.-Y. Pan, J. Yang, and G. V. Chen, Gauge flux generations of weakly magnetized Dirac spin liquid in a kagomé

* chenxray@pku.edu.cn

- [1] O. I. Motrunich, Orbital magnetic field effects in spin liquid with spinon fermi sea: Possible application to $\kappa-(\text{ET})_2\text{cu}_2(\text{CN})_3$, *Phys. Rev. B* **73**, 155115 (2006).
- [2] I. Sodemann, D. Chowdhury, and T. Senthil, Quantum oscillations in insulators with neutral Fermi surfaces, *Phys. Rev. B* **97**, 045152 (2018).
- [3] F. Wu, T. Lovorn, E. Tutuc, and A. H. MacDonald, Hubbard Model Physics in Transition Metal Dichalcogenide Moiré Bands, *Phys. Rev. Lett.* **121**, 026402 (2018).
- [4] J. Zang, J. Wang, J. Cano, and A. J. Millis, Hartree-Fock study of the moiré Hubbard model for twisted bilayer transition metal dichalcogenides, *Phys. Rev. B* **104**, 075150 (2021).
- [5] C. A. Gallegos, R. M. Magaldi, A. Millis, and S. R. White, *Quantum Hall to Chiral Spin Liquid transition in a Triangular Lattice Hofstadter-Hubbard Model* (2025), arXiv:2510.19907 [cond-mat].
- [6] S. Divic, T. Soejima, V. Crépel, M. P. Zaletel, and A. Millis, *Chiral Spin Liquid and Quantum Phase Transition in the Triangular Lattice Hofstadter-Hubbard Model* (2024), arXiv:2406.15348 [cond-mat].
- [7] C. Kuhlenkamp, W. Kadow, A. Imamoglu, and M. Knap, Chiral Pseudospin Liquids in Moiré Heterostructures, *Phys. Rev. X* **14**, 021013 (2024).
- [8] Y. Shen, Y.-D. Li, H. Wo, Y. Li, S. Shen, B. Pan, Q. Wang, H. C. Walker, P. Steffens, M. Boehm, Y. Hao,

lattice, *Phys. Rev. Research* **7**, 043294 (2025).

[25] A. M. Polyakov, Quark confinement and topology of gauge theories, *Nuclear Physics B* **120**, 429 (1977).

[26] F. Becca and S. Sorella, *Quantum Monte Carlo Approaches for Correlated Systems* (Cambridge University Press, Cambridge, 2017).

[27] C. Gros, Physics of projected wavefunctions, *Annals of Physics* **189**, 53 (1989).

[28] Xiao-Tian Zhang, Yong Hao Gao, and Gang Chen, Thermal hall effects in quantum magnets, *Phys. Rep.* **1070**, 1 (2024).

[29] S. Divic, V. Crépel, T. Soejima, X.-Y. Song, A. J. Millis, M. P. Zaletel, and A. Vishwanath, Anyon Superconductivity from Topological Criticality in a Hofstadter-Hubbard Model, *Proc. Natl. Acad. Sci. U.S.A.* **122**, e2426680122 (2025), arXiv:2410.18175 [cond-mat].

[30] F. Chen, W. O. Wang, J.-X. Zhang, L. Balents, and D. N. Sheng, *Topological Chiral Superconductivity in the Triangular-Lattice Hofstadter-Hubbard Model* (2025), arXiv:2509.02757 [cond-mat].

[31] H. Jia, B. Ma, Z. D. Wang, and G. Chen, Quantum spin supersolid as a precursory Dirac spin liquid in a triangular lattice antiferromagnet, *Phys. Rev. Research* **6**, 033031 (2024).

[32] A. Keselman, X. Xu, H. Zhang, C. D. Batista, and O. A. Starykh, *§J_1-J_2§ Triangular Lattice Antiferromagnet in a Magnetic Field* (2025), arXiv:2512.02150 [cond-mat].

[33] T. Bader, S. Feng, S. Budaraju, F. Becca, J. Knolle, and F. Pollmann, *Triangular §J_1-\$J_2§ Heisenberg Antiferromagnet in a Magnetic Field* (2025), arXiv:2512.08768 [cond-mat].

[34] T. Cookmeyer, J. Motruk, and J. E. Moore, Four-Spin Terms and the Origin of the Chiral Spin Liquid in Mott Insulators on the Triangular Lattice, *Phys. Rev. Lett.* **127**, 087201 (2021).

[35] L. Du, Q. Chen, A. D. Barr, A. R. Barr, and G. A. Fiete, Floquet Hofstadter butterfly on the kagome and triangular lattices, *Phys. Rev. B* **98**, 245145 (2018).

[36] A. Wietek, S. Capponi, and A. M. Läuchli, Quantum Electrodynamics in 2 + 1 Dimensions as the Organizing Principle of a Triangular Lattice Antiferromagnet, *Phys. Rev. X* **14**, 021010 (2024).

[37] X.-Y. Song, A. Vishwanath, and Y.-H. Zhang, Doping the chiral spin liquid: Topological superconductor or chiral metal, *Phys. Rev. B* **103**, 165138 (2021).

Supplemental Material for
“Emergent gauge flux and spin ordering in magnetized triangular spin liquids”

Contents

References	5
I. Effective spin model	7
Mean-field phase diagram	8
II. Uniform flux construction in lattice Hamiltonian	8
A. Landau gauge	8
B. Real-space torus gauge	9
III. More discussion on thermal Hall effect	10
IV. Continuum theory of spinon Landau level instability	11
V. Monte Carlo method for projected wavefunction	11

I. Effective spin model

We derive the effective spin Hamiltonian up to order t^4/U^3 for the Hofstadter-Hubbard model with complex hopping amplitudes $t_{ij} = te^{i\varphi_{ij}}$, where the phase φ_{ij} encodes the Peierls phase induced by the orbital magnetic flux. Considering the Hamiltonian of the Hofstadter-Hubbard model,

$$\mathcal{H} = - \sum_{\langle ij \rangle, \sigma} t_{ij} c_{i\sigma}^\dagger c_{j\sigma} + U \sum_i n_{i\uparrow} n_{i\downarrow}, \quad (\text{S1})$$

where $\langle ij \rangle$ denotes nearest-neighbor hopping, σ is the spin degree of freedom, and U is the strength of the local Hubbard repulsion. In the strong-coupling limit ($U \gg t$), the effective Hamiltonian to order t^4/U^3 on the isotropic triangular lattice reads [1, 17, 34]

$$\begin{aligned} \mathcal{H}_{\text{eff}} &= \mathcal{H}_{\text{eff}}^{(2)} + \mathcal{H}_{\text{eff}}^{(3)} + \mathcal{H}_{\text{eff}}^{(4)}, \\ \text{with } \mathcal{H}_{\text{eff}}^{(2)} &= J_1^{(2)} \sum_{\langle ij \rangle} \mathbf{S}_i \cdot \mathbf{S}_j, \\ \mathcal{H}_{\text{eff}}^{(3)} &= J_\chi \sum_{\Delta} \mathbf{S}_1 \cdot \mathbf{S}_2 \times \mathbf{S}_3, \\ \mathcal{H}_{\text{eff}}^{(4)} &= J_1^{(4)} \sum_{\langle ij \rangle} \mathbf{S}_i \cdot \mathbf{S}_j + J_2^{(4)} \sum_{\langle\langle ij \rangle\rangle} \mathbf{S}_i \cdot \mathbf{S}_j \\ &\quad + J_3^{(4)} \sum_{\langle\langle\langle ij \rangle\rangle\rangle} \mathbf{S}_i \cdot \mathbf{S}_j + J_R^{(4)} \sum_{\langle i,j,k,l \rangle} \mathcal{R}_{ijkl}, \\ \text{and } \mathcal{R}_{ijkl} &= (\mathbf{S}_i \cdot \mathbf{S}_j)(\mathbf{S}_k \cdot \mathbf{S}_l) + (\mathbf{S}_i \cdot \mathbf{S}_l)(\mathbf{S}_j \cdot \mathbf{S}_k) - (\mathbf{S}_i \cdot \mathbf{S}_k)(\mathbf{S}_j \cdot \mathbf{S}_l). \end{aligned} \quad (\text{S2})$$

The antiferromagnetic interactions $J_1^{(2),(4)}$, $J_2^{(4)}$, $J_3^{(4)}$, J_χ and $J_R^{(4)}$ denote the first-, second-, third-neighbor and 3-site-ring, 4-site-ring exchange couplings, with

$$\begin{aligned} J_1^{(2)} &= \frac{4t^2}{U}, \quad J_1^{(4)} = -\frac{24t^4}{U^3}, \quad J_2^{(4)} = J_3^{(4)} = \frac{4t^2}{U^3}, \\ J_\chi &= -\frac{24t^3}{U^2} \sin(\Phi_\Delta), \quad J_R^{(4)} = \frac{80t^4}{U^3}. \end{aligned} \quad (\text{S3})$$

where dimensionless flux Φ_Δ is defined as the sum of the Peierls phases around the triangle Δ .

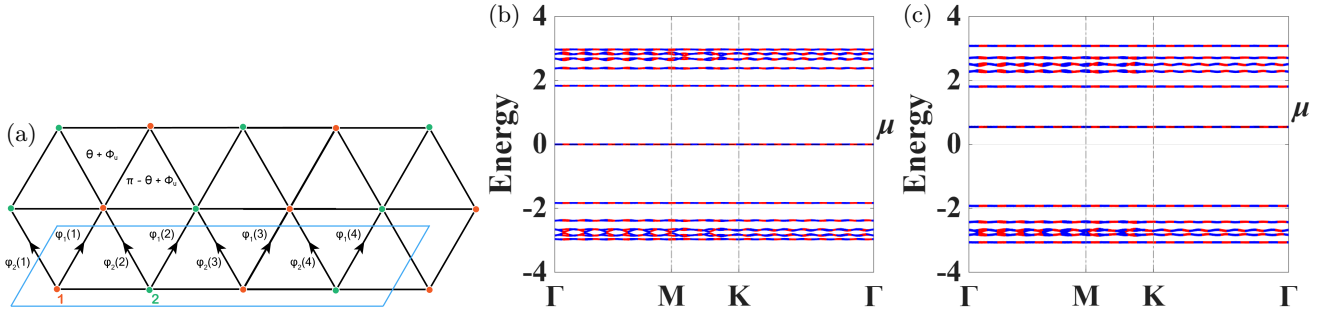


FIG. S1. (a) Combined flux pattern on the triangular lattice. For uniform gauge flux $\phi_u = 2\pi p/(4q)$ threading through the triangular plaquettes, we define the Peierls phases as $\varphi_1(l, s) = \phi_u[2(2(l-1)+s)-1/2]$ and $\varphi_2(l, s) = \phi_u[2(2(l-1)+s)+1/2]$, with sublattice index $s = 1, 2$. The magnetic unit cell is enlarged and contains $2q$ sites due to magnetic translational symmetry. For example, the cyan parallelogram shows the enlarged magnetic unit cell for flux $\phi_u = 2\pi/(4q)$ with $q = 2$. Within each unit cell, sublattice sites are labeled as 1 (even) and 2 (odd) according to the spin liquid flux pattern. Spinon band structures for uniform flux $\phi_u = 2\pi/(4 \times 11)$ with staggered flux $\theta = 0$ (panel b) and $\theta = \pi/6$ (panel c), respectively. For $\theta = 0$ (panel b) the original two Chern bands split into 11 pairs of degenerate subbands with Chern numbers $[-2, 9, -2, -2, -2, -2, -2, -2, 9, -2]$, while for $\theta = \pi/6$ (panel c) the sequence becomes $[-2, 9, -2, -2, -2, -2, -2, -2, 9, -2, -2]$.

In reality, one can apply the external magnetic field away from the z direction. The z component contributes to the orbital magnetic flux, and the total magnetic field contributes to the Zeeman coupling. As the effective spin model with the ring exchange has the global SU(2) symmetry, the presence of the Zeeman coupling in the effective model breaks the SU(2) symmetry down to U(1), and then the Zeeman coupling can be conveniently set to be along z direction in the spin space.

Mean-field phase diagram

We perform the mean-field calculations of the effective spin model \mathcal{H}_{eff} with J_1 , J_2 and J_χ , using the fermionic parton construction described in the main text. The mean-field phase diagram in the J_χ - B plane with fixed $J_1 = 1$ and $J_2 = 0.1$ is shown in Fig. 3(b). When both J_χ and B vanish, the ground state corresponds to a U(1) DSL [19, 20]. In the absence of magnetic field, increasing J_χ from zero drives the DSL into a CSL. This CSL remains stable up to a critical field B_c , above which the system transitions to the LL state. The staggered flux parameter θ for different J_χ at phase boundary is in agreement with the variational Monte Carlo results of Ref. [22], and the critical field B_c is determined by the closing of the spinon gap in the CSL phase.

II. Uniform flux construction in lattice Hamiltonian

A. Landau gauge

To incorporate a uniform flux ϕ_u per triangle into the triangular lattice, we can choose the Landau gauge. In this gauge, the non-trivial Peierls phases for nearest-neighbor hopping are defined as $\varphi_1(i) = \phi_u(2 \cdot \mathbf{r}_i - 1/2)$ along the \mathbf{a}_2 direction, and $\varphi_2(i) = \phi_u(2 \cdot \mathbf{r}_i + 1/2)$ along the $\mathbf{a}_3 = \mathbf{a}_2 - \mathbf{a}_1$ direction [35]. With coprime integers p and q , the uniform flux $\phi_u = 2\pi p/(2q)$ threads each elementary triangle (either Δ or ∇), resulting in an enlarged magnetic unit cell along the \mathbf{a}_1 direction that contains q sites.

Additionally, considering the spin liquid two-sublattice flux pattern illustrated in Fig. S1(a), the corresponding Hamiltonian can be expressed as $H(\theta, \phi_u) = -t \sum_{\mathbf{k}} \mathcal{H}_{\mathbf{k}}^{(1)} + \mathcal{H}_{\mathbf{k}}^{(2)} + \mathcal{H}_{\mathbf{k}}^{(3)} + h.c.$ with

$$\mathcal{H}_{\mathbf{k}}^{(1)} = \sum_{l=1}^{q_{db}} f_{l,1}^\dagger f_{l,1} e^{i\mathbf{k} \cdot \mathbf{a}_2} e^{-i\varphi_1(l,1)} + f_{l,2}^\dagger f_{l,2} e^{i\mathbf{k} \cdot \mathbf{a}_2} e^{i\pi} e^{-i\varphi_1(l,2)} \quad (S4)$$

$$\mathcal{H}_{\mathbf{k}}^{(2)} = \sum_{l=1}^{q_{db}} f_{l,1}^\dagger f_{l,2} e^{i\theta} + \sum_{l=1}^{q_{db}-1} f_{l,2}^\dagger f_{l+1,1} e^{i\theta} + f_{q_{db},2}^\dagger f_{1,1} e^{i\mathbf{k} \cdot \mathbf{q}_{db} \cdot 2\mathbf{a}_1} e^{i\theta} \quad (S5)$$

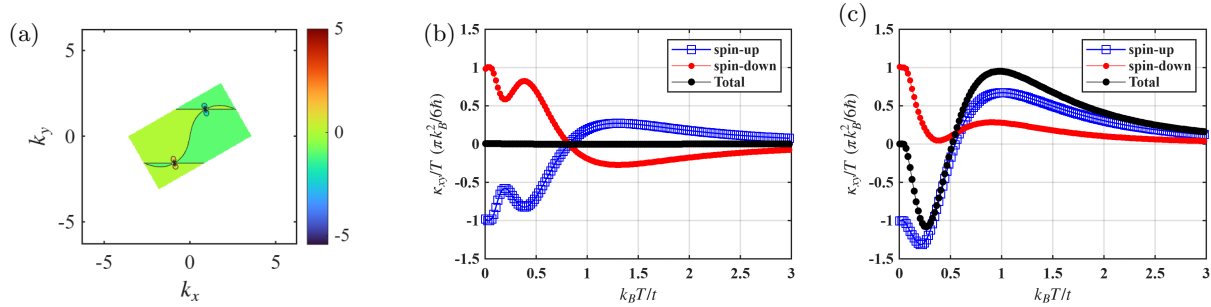


FIG. S2. (a) Berry curvature distribution of the Dirac spin liquid with uniform flux $\phi_u = 0$ and Zeeman coupling $B = 0$. (b) Thermal Hall response with uniform flux $\phi_u = 2\pi/76$, staggered flux $\theta = 0$ and $B = 1$. (c) Similar to (b), but with $\theta = \pi/6$.

$$\begin{aligned} \mathcal{H}_{\mathbf{k}}^{(3)} = & f_{1,1}^\dagger f_{q_{db},2} e^{i\mathbf{k} \cdot (-q_{db} \cdot 2\mathbf{a}_1 + \mathbf{a}_2)} e^{-i\pi/2} e^{-i\varphi_2(l=1,1)} + \sum_{l=2}^{q_{db}} f_{l,1}^\dagger f_{l-1,2} e^{i\mathbf{k} \cdot \mathbf{a}_2} e^{-i\pi/2} e^{-i\varphi_2(l,1)} \\ & + \sum_{l=1}^{q_{db}} f_{l,2}^\dagger f_{l,1} e^{i\mathbf{k} \cdot \mathbf{a}_2} e^{i\pi/2} e^{-i\varphi_2(l,2)} \end{aligned} \quad (S6)$$

where $\varphi_1(l, s) = \phi_u[2 \cdot (2(l-1) + s) - 1/2]$, and $\varphi_2(l, s) = \phi_u[2 \cdot (2(l-1) + s) + 1/2]$, with $\phi_u = 2\pi p/(4q)$ and sublattice index $s = 1, 2$. In this combined flux effect, the enlarged magnetic unit cell has instead $2q$ sites. The energy spectrum is obtained by numerically diagonalizing the $2q \times 2q$ Hamiltonian matrix for each wave vector \mathbf{k} . Therefore, the original Chern bands split into several magnetic subbands with high flatness and different Chern numbers as shown in Fig. S1(b,c).

B. Real-space torus gauge

While continuum magnetic fields are often implemented using Landau or symmetric gauges, such choices are ill-suited for finite lattice systems with periodic boundary conditions. To describe a situation in which only a single flux quantum threads the entire system in real space—a setup essential for Monte Carlo simulations—we instead adopt a real-space torus gauge. In this construction, the gauge field is defined directly on lattice bonds of an $L_x \times L_y$ torus, ensuring a uniform flux Φ_u through every triangular plaquette while maintaining exact periodicity.

However, to consider a scenario where only a single flux quantum penetrates the entire lattice system in real space [36], a different gauge choice is required—one that is essential for Monte Carlo calculations. We construct a gauge field A_{ij} on a torus ($L_x \times L_y$) to generate a uniform flux Φ_u per triangular plaquette. The bond phase θ_{ij} for a hopping from site $i = (n_1, n_2)$ to j depends on the bond direction \mathbf{d} and boundary conditions. We define phase increments $\delta_1 = 4\Phi_u$ and $\delta_2 = 2\Phi_u$.

1. Horizontal Bonds ($\mathbf{d} = \mathbf{a}_1$)

$$\theta(\mathbf{r}, \mathbf{a}_1) = \begin{cases} (n_1 - 1)\delta_1 + (n_2 - 1)\delta_2 & \text{Bulk} \\ (L_x - 1)\delta_1 - (n_2 - 1)((L_x - 1)\delta_1 + 2\Phi_u) & \text{Boundary } (n_1 = L_x) \end{cases} \quad (S7)$$

2. Vertical Bonds ($\mathbf{d} = \mathbf{a}_2$)

$$\theta(\mathbf{r}, \mathbf{a}_2) = \begin{cases} (n_2 - 1)\delta_2 + (n_1 - 1)\delta_1 - \Phi_u & \text{Bulk} \\ ((L_y - 1)\delta_2 - \Phi_u) - (n_1 - 1)((L_y - 1)\delta_2 - 2\Phi_u) & \text{Boundary } (n_2 = L_y) \end{cases} \quad (S8)$$

3. Diagonal Bonds ($\mathbf{d} = \mathbf{a}_2 - \mathbf{a}_1$)

$$\theta(\mathbf{r}, \mathbf{a}_3) = \begin{cases} 0 & \text{Bulk} \\ (n_2 - 1)(\theta_{\mathbf{a}_2}(L_x, 2) + 3\Phi_u) & \text{Left Edge } (n_1 = 1, 1 < n_2 < L_y) \\ -(n_1 - 2)(\theta_{\mathbf{a}_1}(2, L_y - 1) - 2\Phi_u) & \text{Top Edge } (n_2 = L_y, n_1 > 1) \\ \theta_{\mathbf{a}_2}(1, L_y) - \theta_{\mathbf{a}_1}(L_x, 1) - \Phi_u & \text{Top-Left Corner } (n_1 = 1, n_2 = L_y) \end{cases} \quad (S9)$$

This gauge choice ensures uniform flux Φ_u through all plaquettes on the torus.

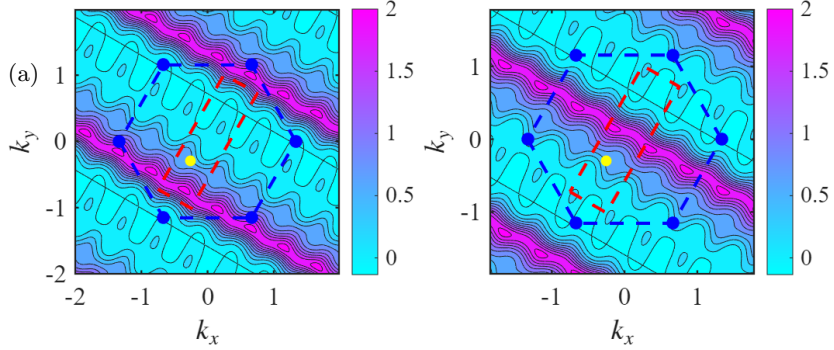


FIG. S3. Berry curvature distribution of the first (a) and fourth (b) magnetic subbands in the LL state with uniform flux $\phi_u = 2\pi/8$. The Chern numbers of these two subbands both are $C = 1$. And the yellow points denote the shifted inversion centers in the magnetic Brillouin zone.

III. More discussion on thermal Hall effect

The absence of a finite thermal Hall response in a U(1) Dirac spin liquid is rooted in the symmetry-constrained structure of the spinon Berry curvature. In the Dirac spin liquid, the low-energy spinon spectrum consists of a pair of massless Dirac cones located at symmetry-related momenta in the Brillouin zone. Although each Dirac point carries a quantized Berry phase, the associated Berry curvature is singular and localized at the Dirac nodes, vanishing elsewhere in the momentum space. As a result, the Berry curvature contributions from different Dirac cones cancel exactly upon Brillouin-zone integration. Moreover, time-reversal symmetry enforces an odd transformation of the Berry curvature, $\Omega(\mathbf{k}) = -\Omega(-\mathbf{k})$ in Fig. S2(a), while the spinon occupation remains uniform in momentum space. Consequently, the Berry-curvature-weighted integral governing intrinsic Hall-type responses vanishes identically. It is worth mentioning that DSL Hamiltonian has symmetric spectrum due to particle-hole symmetry, i.e. $PH(\mathbf{k})P^{-1} = -H(-\mathbf{k})$ with $P = i\sigma_y K$. This symmetry ensures that for every state at energy ϵ there exists a corresponding state at energy $-\epsilon$.

Now we first turn to the Fermi-pocket state with a finite Zeeman coupling. Upon introducing a Zeeman coupling B that breaks time-reversal, the spinon bands split into the Fermi-pocket state, but the overall symmetric Berry curvature remain unchanged and each bands are equally filled under the chemical potential. Each spin sector still hosts Dirac cones with opposite Berry curvature distributions, leading to a continued cancellation in the total thermal Hall conductivity. Thus, even with a finite B , the Fermi-pocket state maintains a zero thermal Hall response due to the fundamental symmetry constraints on its Berry curvature structure.

Next we discuss the LL state after including the spontaneous flux generation. With a uniform flux ϕ_u and Zeeman coupling B , the spinon bands in the Dirac spin liquid split into multiple Hofstadter-like subbands for LL state, each characterized by distinct Chern numbers in Fig. S1(b). Although each spin sector individually acquires a finite thermal Hall response (blue and red lines) in Fig. S2(b), the total thermal Hall conductivity (black line) vanishes at all temperatures. This can be understood once the Hall coefficient σ_{xy} is analyzed to be an odd function of energy. By definition,

$$\begin{aligned} \sigma_{xy}(\epsilon) &= -\sum_n \sum_{\epsilon_{n\mathbf{k}} < \epsilon} \Omega_{n\mathbf{k}}(\epsilon_{n\mathbf{k}}) = -\int_{-\infty}^{\epsilon} d\gamma \int_{\epsilon_{\mathbf{k}}=\gamma} \frac{d^2\mathbf{k}}{(2\pi)^2} \Omega_{\mathbf{k}}(\epsilon_{\mathbf{k}}), \\ \sigma_{xy}(-\epsilon) &= -\int_{-\infty}^{-\epsilon} d\gamma \int_{\epsilon_{\mathbf{k}}=\gamma} \frac{d^2\mathbf{k}}{(2\pi)^2} \Omega_{\mathbf{k}}(\epsilon_{\mathbf{k}}) = -\int_{\epsilon}^{\infty} d\gamma \int_{\epsilon_{\mathbf{k}}=-\gamma} \frac{d^2\mathbf{k}}{(2\pi)^2} \Omega_{\mathbf{k}}(\epsilon_{\mathbf{k}}). \end{aligned} \quad (\text{S10})$$

where, for simplicity, we absorb the subband index n into the continuous energy variable γ . For the LL state derived from the DSL, we numerically find that for every $\Omega_{\mathbf{k}}(\epsilon_{\mathbf{k}})$ with energy $\epsilon_{\mathbf{k}} = \gamma$, there exists a corresponding $\Omega_{\bar{\mathbf{k}}}(\epsilon_{\bar{\mathbf{k}}}) = \Omega_{\mathbf{k}}(\epsilon_{\mathbf{k}})$ with energy $\epsilon_{\bar{\mathbf{k}}} = -\gamma$, leading to the equavalant contribution for the momentum integral. And the momenta \mathbf{k} and $\bar{\mathbf{k}}$ can be related by a shifted inversion center (yellow points) in the Brillouin zone in the S3. This special property should be related to the underlying gauge symmetries realized in the LL state, which we defer for future study. Therefore one can prove $\sigma_{xy}(\epsilon)$ is an odd function of energy ϵ from the addition of two equations in Eq. (S10) and the fact that the total Berry curvature, i.e. Chern number, is zero. Under finite Zeeman splitting, while the individual contributions $\sigma_{xy}^{\pm} \equiv \sigma_{xy}(\epsilon \pm E_{\text{Zeeman}})$ for spin- \uparrow and spin- \downarrow spinons are neither strictly even nor odd, their sum $\sigma_{xy}^{\text{tot}} = \sigma_{xy}^+ + \sigma_{xy}^-$ remains an odd function of energy. Consequently, when integrated over energy

with the remaining even-function factors in Eq. (4), the total thermal Hall conductivity vanishes identically at any temperature.

While the vanishing thermal Hall conductivity in the LL state can be attributed to the underlying symmetries of this special LL state, this cancellation is not generic for all flux states. Especially, the chiral spin liquid phase breaks time-reversal symmetry intrinsically, leading to an asymmetric distribution of Berry curvature among the Hofstadter subbands. This asymmetry allows for a finite thermal Hall conductivity, as shown in Fig. S2(c) and Fig. 5(b). And also, further neighbor hopping terms may break the special symmetry in LL state, resulting in a finite thermal Hall conductivity.

IV. Continuum theory of spinon Landau level instability

Based on aforementioned discussions, the low-energy physics can be effectively described by Dirac cones near the chemical potential in Fig. 2. For illustration, we take the low-energy continuum theory of Dirac fermion with gauge field \mathbf{a} as [37]

$$\mathcal{H} = v_f [(q_x - a_x)\sigma_x + (q_y - a_y)\sigma_y] + m\sigma_z, \quad (\text{S11})$$

where v_f is the Fermi velocity, and m is the mass of the Dirac fermions. Note that Eq. (S11) is applicable for both Dirac cones, and Zeeman splitting of spinons has not yet been included. Taking Landau gauge $\mathbf{a} = (0, -xb)$ with $\mathbf{b} = -be_z$ and $b > 0$, we obtain Landau level spectrum, $\mathcal{E}_n = \text{sgn}(n)\omega_D \sqrt{\Delta^2 + |n|}$ for $n = \pm 1, \pm 2, \dots$, and $\mathcal{E}_0 = \omega_D \Delta$ for $n = 0$. Here, $\omega_D = \sqrt{2b}v_f$ is the characteristic energy scale of the Landau levels. Due to finite Zeeman field, the spin- \uparrow and spin- \downarrow spinons have different chemical potentials, $\mu_\uparrow > \mu_\downarrow$. Thus, the magnetization density is $m_z = \frac{N_\uparrow - N_\downarrow}{A} = 2\frac{b}{2\pi}$, where N_\uparrow, N_\downarrow are the number of up and down spins, and A is the system area. Therefore, the 0-th Landau level is tuned to be fully filled for spin- \uparrow spinons, while it is empty for spin- \downarrow spinons, in Fig. 3, which is denoted as the LL state.

In this mean field picture, the energy cost under magnetic field for LL and FP states from the massless DSL state ($m = 0$) can be calculated straightforwardly, i.e., $\Delta\mathcal{E}_{\text{LL(FP)}} = \mathcal{E}_{\text{LL(FP)}} - \mathcal{E}_{\text{DSL}} - bm_z$, where \mathcal{E}_{LL} , \mathcal{E}_{FP} and \mathcal{E}_{DSL} are the mean-field energies density. As a result, we find that

$$\frac{\Delta\mathcal{E}_{\text{LL}}}{\Delta\mathcal{E}_{\text{FP}}} = \frac{3\sqrt{2} \left[-\frac{2|\Delta|^3}{3} - \zeta(-\frac{1}{2}, 1 + \Delta^2) - \frac{|\Delta|}{2} \right]}{(1 + 2\Delta^2)^{\frac{3}{2}} - (2\Delta^2)^{\frac{3}{2}}}, \quad (\text{S12})$$

where $\zeta(x, y)$ is the Zeta function. The ratio $\Delta\mathcal{E}_{\text{LL}}/\Delta\mathcal{E}_{\text{FP}}$ increases monotonically with increasing $|\Delta|$, which is always larger than 1. Thus, the LL state has lower mean-field energy than the FP state, which is consistent with our numerical results in Fig. 2(d) and previous studies on Kagomé lattice [23, 24].

V. Monte Carlo method for projected wavefunction

To determine the ground state energy and characterize potential spin ordering under Gutzwiller projection, we employ the Monte Carlo sampling [26, 27]. The approach is based on evaluating the expectation value of an operator \hat{O} with respect to a given wavefunction $|\Psi\rangle$:

$$\langle \hat{O} \rangle = \frac{\langle \Psi | \hat{O} | \Psi \rangle}{\langle \Psi | \Psi \rangle} = \frac{\sum_x \langle \Psi | x \rangle \langle x | \hat{O} | \Psi \rangle}{\sum_x \langle \Psi | x \rangle \langle x | \Psi \rangle}, \quad (\text{S13})$$

where $|x\rangle$ is a complete set of basis. Theoretically, if we can enumerate all the basis states $|x\rangle$, we can calculate the expectation value exactly. However, in practice, the Hilbert space is usually exponentially large with the number of particles, making the exact calculation infeasible. Therefore, we resort to Monte Carlo method to carry out importance sampling, and the key step is to rewrite the expectation value as

$$\langle \hat{O} \rangle = \sum_x P(x) O_L(x), \quad P(x) = \frac{|\langle x | \Psi \rangle|^2}{\sum_{x'} |\langle x' | \Psi \rangle|^2}, \quad (\text{S14})$$

where we introduce the local estimator of the operator \hat{O} :

$$O_L(x) = \frac{\langle x | \hat{O} | \Psi \rangle}{\langle x | \Psi \rangle} = \sum_{x'} \langle x | \hat{O} | x' \rangle \frac{\langle x' | \Psi \rangle}{\langle x | \Psi \rangle}. \quad (\text{S15})$$

It is straightforward to verify that $P(x)$ is a normalized probability distribution. We can therefore sample the basis states $|x\rangle$ according to $P(x)$ using the Markov Chain Monte Carlo (MCMC) method, generating a sequence of samples $\{x_i\}$ that follow this distribution. The expectation value is then calculated as the average of the local estimator:

$$\langle \hat{O} \rangle \approx \frac{1}{N} \sum_{i=1}^N O_L(x_i). \quad (\text{S16})$$

In our studied case, we use the Gutzwiller projected mean-field wavefunction as the trial wavefunction $|\Psi\rangle$, which is constructed from a mean-field Hamiltonian that captures the essential physics of the system. More specifically, we start from a mean-field Hamiltonian Eq. (2), and obtain its ground state wavefunction $|\Psi_{\text{MF}}\rangle$ via diagonalizing. Finally, we apply the Gutzwiller projection operator $P = \prod_i (1 - n_{i\uparrow} n_{i\downarrow})$ to enforce the single-occupancy constraint, resulting in the wavefunction $|\Psi\rangle = P |\Psi_{\text{MF}}\rangle$. To incorporate the uniform flux in Monte Carlo calculations, we adopt the gauge construction detailed in Sec. II B. This gauge choice ensures that the uniform flux ϕ_u threading the lattice is self-consistently related to the finite magnetization, i.e., $\phi_u = (2\pi)m_z/2$, which is also consistent with the continuum theory analysis.